

Turbulence Dynamo in the Stratified Medium of Galaxy Clusters

SOONYOUNG ROH,¹ DONGSU RYU,¹ HYESUNG KANG,² SEUNGWOO HA,¹ AND HANBYUL JANG¹

¹*Department of Physics, School of Natural Sciences, UNIST, Ulsan 44919, Korea*

²*Department of Earth Sciences, Pusan National University, Busan 46241, Korea*

(Received; Revised; Accepted)

Submitted to The Astrophysical Journal

ABSTRACT

The existence of microgauss magnetic fields in galaxy clusters have been established through observations of synchrotron radiation and Faraday rotation. They are conjectured to be generated via small-scale dynamo by turbulent flow motions in the intracluster medium (ICM). Some of giant radio relics, on the other hand, show the structures of synchrotron polarization vectors, organized over the scales of \sim Mpc, challenging the turbulence origin of cluster magnetic fields. Unlike turbulence in the interstellar medium, turbulence in the ICM is subsonic. And it is driven sporadically in highly stratified backgrounds, when major mergers occur during the hierarchical formation of clusters. To investigate quantitatively the characteristics of turbulence dynamo in such ICM environment, we performed a set of turbulence simulations using a high-order-accurate, magnetohydrodynamic (MHD) code. We find that turbulence dynamo could generate the cluster magnetic fields up to the observed level from the primordial seed fields of 10^{-15} G or so within the age of the universe, if the MHD description of the ICM could be extended down to \sim kpc scales. However, highly organized structures of polarization vectors, such as those observed in the Sausage relic, are difficult to be reproduced by the shock compression of turbulence-generated magnetic fields. This implies that the modeling of giant radio relics may require the pre-existing magnetic fields organized over \sim Mpc scales.

Keywords: galaxies: clusters: intracluster medium – magnetic fields – methods: numerical – shock waves – turbulence

1. INTRODUCTION

The baryonic matter in galaxy clusters resides mostly in the intracluster medium (ICM), in the form of hot diffuse plasma. The ICM is known to be highly dynamic and turbulent (Brunetti & Jones 2014, and references therein). In addition, the ICM contains the magnetic fields of μ G-level, corresponding to the energy density of the order of ~ 1 % of the thermal energy density, throughout the whole volume of clusters, as revealed in observations of diffuse synchrotron emissions from radio halos and relics and Faraday rotation measures (e.g., Govoni & Feretti 2004; Feretti et al. 2012).

Magnetic fields play important roles in the ICM, particularly governing microphysical processes, such as the

turbulent acceleration of cosmic rays (CRs) and the formation of shock waves, as well as thermal conduction and kinetic viscosity (e.g., Brunetti & Lazarian 2007; Kunz et al. 2010; Guo et al. 2014; Roberg-Clark et al. 2016; Ha et al. 2018b). Yet, the nature and origin of cluster magnetic fields have not yet been fully understood. It was suggested that “turbulence dynamo” may be responsible for the generation of ICM magnetic fields, at least in the outskirts (e.g., Ryu et al. 2008; Porter et al. 2015). Turbulence dynamo, which refers to the amplification of weak seed magnetic fields by turbulent flow motions, generates random fields on scales smaller than the driving scale of turbulence, and hence is often called small-scale dynamo (e.g., Batchelor 1950; Kazantsev 1968; Cho & Vishniac 2000; Schekochihin et al. 2004; Cho et al. 2009). Typically, it goes through three stages, the initial exponential growth when the magnetic field is dynamically negligible on all scales, the follow-up linear

growth when the magnetic energy becomes comparable to the kinetic energy at the dissipation scale, and finally the saturation stage when the magnetic energy accounts for a substantial fraction of the turbulent energy.

Seed fields for cluster magnetic fields, however, are unknown and varied, although many candidates, ranging from primordial to plasma physical, and astrophysical, have been suggested (e.g., [Ryu et al. 2012](#); [Widrow et al. 2012](#), for reviews). Fermi-LAT observations of blazars set a lower bound of $\sim 10^{-16} - 10^{-15}$ G at the scale of ~ 1 Mpc for void magnetic fields (e.g., [Neronov & Vovk 2010](#); [Tavecchio et al. 2010](#)). Planck observations of cosmic microwave background (CMB) anisotropies put a strong upper limit of $B \lesssim 10^{-9}$ G again at the scale of ~ 1 Mpc (comoving strength and scale) for the primordial field strength ([Planck Collaboration 2016](#)). Hence, the initial seed fields for cluster magnetic fields would be many orders of magnitude weaker than the observed fields of $\sim \mu\text{G}$ strength.

Turbulence, and hence ensuing dynamo, in galaxy clusters differ significantly from those in other astrophysical environments, such as molecular clouds and star-forming regions. For instance, the ICM turbulence is induced in highly stratified backgrounds, and driven sporadically by mergers during the hierarchical formation of the large-scale structure (LSS) of the universe (e.g., [Miniati 2015](#); [Vazza et al. 2017](#)). In addition, while supersonic turbulence is common in astrophysical environments, the ICM turbulence is expected to be subsonic with turbulence Mach number $M_{\text{turb}} \sim 1/2$ or so (e.g., [Ryu et al. 2008](#); [Porter et al. 2015](#)).

Magnetic field amplification in the ICM have been studied by several authors, using cosmological magnetohydrodynamic (MHD) simulations for the LSS formation (e.g., [Vazza et al. 2014](#); [Marinacci et al. 2015](#); [Vazza et al. 2018](#)). In turbulence dynamo, the initial exponential growth is rapid, so the memory of seed field properties, such as the strength and length scale, is supposed to be lost. However, the aforementioned studies using cosmological MHD simulations so far have shown that the amplification of magnetic fields due to turbulence dynamo alone (without radiative cooling and feedback processes) is limited. Hence, in order to amplify seed fields via turbulence dynamo to the observed strength of $\sim \mu\text{G}$ in clusters, the void fields have to be around nanogauss, which is stronger than that inferred from other observations mentioned above. This indicates that either turbulence dynamo may not be the main mechanism that amplifies the ICM magnetic fields, or these cosmological simulations may not have fully reproduced turbulence dynamo in the ICM, perhaps owing to insufficient grid resolution.

In the outskirts of galaxy clusters, the so-called radio relics, elongated structures of diffuse synchrotron emission, have been observed (e.g., [Brüggen et al. 2012](#); [Ferretti et al. 2012](#), for reviews). They are thought to be associated with ICM shocks of Mach number $M_s \sim 2 - 3$, induced by mergers (e.g., [van Weeren et al. 2019](#), for review). The synchrotron radiation is polarized with average polarization fraction $\sim 10 - 30\%$, and the polarization vectors are aligned with the shock normal. A spectacular example is the Sausage relic in cluster CIZA J2242.8+5301 ([van Weeren et al. 2010](#)). It shows a very high polarization fraction of $\sim 50 - 60\%$ with highly aligned polarization vectors over its length of ~ 2 Mpc. These radio relics may indicate the presence of the magnetic fields coherent over $\sim \text{Mpc}$ scales in the cluster outskirts, possibly challenging the small-scale, turbulence dynamo origin of cluster magnetic fields.

In this paper, we investigate whether turbulence dynamo could be the mechanism for the generation of observed magnetic fields in galaxy clusters. We first check whether the cluster magnetic fields of $\sim \mu\text{G}$ strength could emerge from very weak seed fields, consistent with the inferred lower bound of the void fields. We also examine whether the structures of synchrotron polarization vectors observed in radio relics could be explained by the compression of turbulence-generated magnetic fields across weak ICM shocks.

Toward that end, instead of cosmological structure-formation simulations, we employ turbulence simulations in a controlled periodic volume. To model the realistic cluster environment, the background medium is stratified radially in hydrostatic equilibrium with an external gravity, and the turbulence is driven sporadically mimicking major mergers as described above. Some aspects of turbulence and dynamo in the stratified background were previously investigated. For instance, [Shi et al. \(2018\)](#) discussed the behavior of the hydrodynamic turbulence influenced by the buoyancy of the stratified ICM, using cosmological structure-formation simulations. [Jabbari et al. \(2014\)](#) examined the magnetic field evolution in the mean-field dynamo of stellar convection. However, the effects of the background stratification on small-scale dynamo by turbulent flow motions have not yet been fully explored and quantified.

We here employ an MHD simulation code with high-order accuracy, which performs better for the amplification of magnetic field. Our simulation results can be directly compared to previous turbulence simulations, in which the background medium is uniform and the turbulence forcing is continuous in time. And we will test numerically-converged results with sufficient grid resolutions. The paper is organized as follows. Numerical

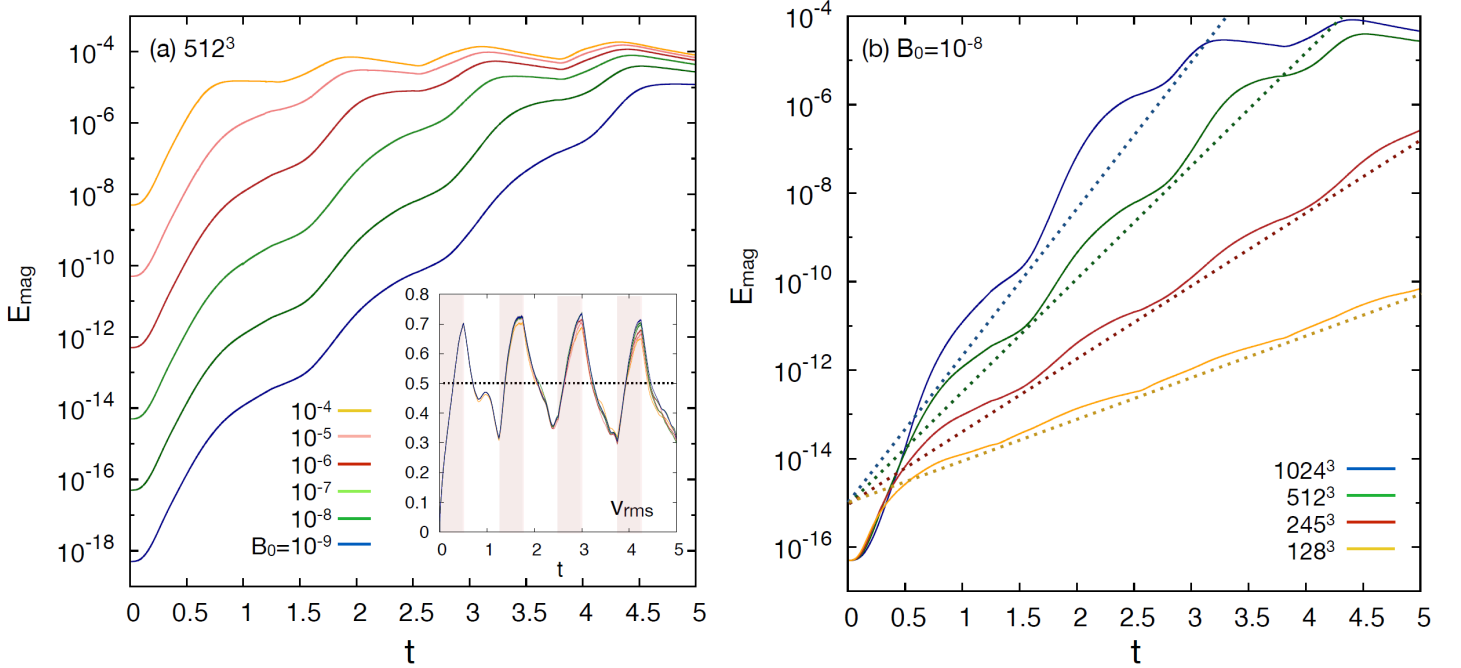


Figure 1. Magnetic field amplification in turbulence dynamo. (a) The evolution of the magnetic energy, $E_{\text{mag}} = (1/2)B^2$, with different seed fields of $B_0 = 10^{-9}$ to 10^{-4} in simulations using 512^3 grid zones. The evolution of the rms flow velocity, $v_{\text{rms}} \equiv \langle v^2 \rangle^{1/2}$, is shown in the inserted box; the lines of different colors almost overlap. (b) The evolution of E_{mag} with $B_0 = 10^{-8}$ in simulations using different numbers of grid zones. Dashed lines show the fittings of the late exponential growth (see the text). Here, $B = 1$ is equivalent to $\sim 5 \times 10^{-5}$ G and $t_{\text{end}} = 5$ to 13 Gyrs, if the model parameters are scaled to the physical parameters relevant for the Coma cluster.

setups and simulations are outlined in Section 2. Results are described in Section 3. A brief summary follows in Section 4.

2. SIMULATIONS

We carried out simulations by solving equations for isothermal, compressible MHD flows, where the gas pressure is modeled as $P_g \equiv \rho c_s^2$ with a constant sound speed c_s . A three-dimensional (3D) code based on the MHD version (Jiang & Wu 1999) of a weighted essentially non-oscillatory (WENO) scheme (Jiang & Shu 1996) was employed. The eigenvalues and eigenvectors of isothermal MHD flows in Kim et al. (1999) were implemented. With a 4th-order RungeKutta (RK) scheme for the time evolution, the code has a 5th-order spatial accuracy and a 4th-order temporal accuracy. The $\nabla \cdot \mathbf{B} = 0$ constraint was enforced using a constrained transport (CT) scheme (Ryu et al. 1998). Viscous and resistive dissipations are not explicitly modeled.

Conventional MHD turbulence simulations adopt a periodic volume in an initially uniform background. Here, we consider a periodic simulation box that contains a spherically symmetric halo with the stratified gas distribution. To emulate the ICM distribution of galaxy clusters, the background medium is modeled by an isothermal β distribution (e.g., Cavaliere & Fusco-

Femiano 1976) as follows:

$$\rho(r) = \rho_0 \left[1 + \left(\frac{r}{r_c} \right)^2 \right]^{-3\beta/2}, \quad (1)$$

where the center of the simulation box is located at $r = 0$. The dimensionless gas density and pressure are initialized with $\rho_0 = 1$ and $P_{g,0} = 1$ (so $c_s = 1$) in simulation units, respectively. We set $\beta = 1$ and $r_c = 0.075$. Simulations were performed in a cubic box of dimensionless size $L_0 = 1$, using $N_g^3 = 128^3$ to 1024^3 grid zones.

An external gravity balancing the pressure gradient due to the stratification, $g = c_s^2 d \ln \rho / dr$, is added to the momentum equation. Initially, the medium is at rest with $\mathbf{v} = 0$, and the computational volume is permeated with a uniform magnetic field of $\mathbf{B}_0 = (B_0, 0, 0)$ parallel to the \hat{x} -axis; a range of $B_0 = 10^{-9} - 10^{-4}$ is considered.¹

Turbulence is driven with “solenoidal” forcing, i.e., $\nabla \cdot \delta \mathbf{v} = 0$. The velocity perturbations, $\delta \mathbf{v}$, are drawn from a Gaussian random field of power spectrum, $|\delta v_k|^2 \propto k^6 \exp(-8k/k_{\text{inj}})$ with $k_{\text{inj}} = 8k_0$ ($k_0 = 2\pi/L_0$),

¹ The unit of \mathbf{B} is chosen so that the magnetic energy is given as $E_{\text{mag}} = (1/2)B^2$.

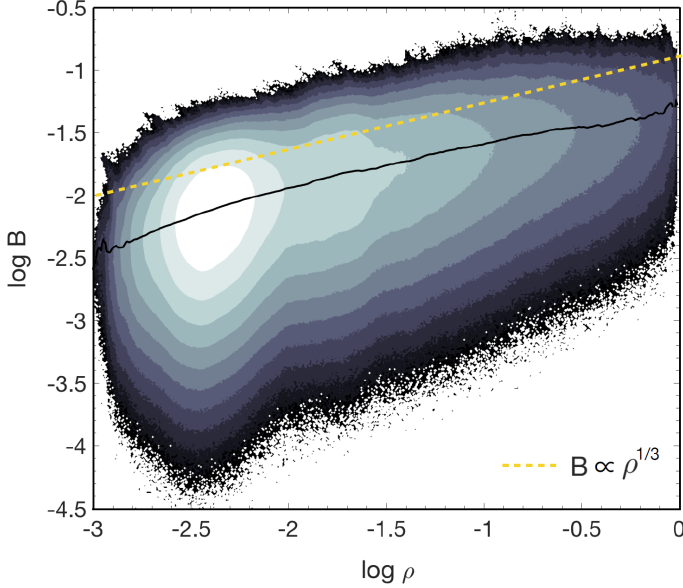


Figure 2. Correlation between the gas density and the magnetic field strength at $t = 4.6$ in the high-resolution simulation of 1024^3 grid zones with the initial background magnetic field strength of $B_0 = 10^{-8}$. The black solid line shows the average magnetic field strength, and the yellow dashed line draws the $B \propto \rho^{1/3}$ scaling relation.

and added to \mathbf{v} (e.g., Stone et al. 1998; Mac Low 1999). They have random phases, so the driving is temporally uncorrelated. Unlike other conventional turbulence simulations where the forcing is applied continuously in time, the velocity perturbations are enforced “sporadically”, mimicking major merger events in galaxy clusters. Considering each cluster suffers a few to several major mergers (e.g., Miniati 2015; Vazza et al. 2017), the forcing is turned on for the duration of $\Delta t_{\text{on}} = 0.5$ and off for $\Delta t_{\text{off}} = 0.75$, 4 times until the end of simulations at $t_{\text{end}} = 5$.

The amplitude of the forcing is tuned, so that $v_{\text{rms}} \equiv \langle v^2 \rangle^{1/2}$ is in the range of $\sim 0.3 - 0.7$ with a mean of $\sim 1/2$. With $c_s = 1$, the mean turbulence Mach number is $M_{\text{turb}} \equiv v_{\text{rms}}/c_s \sim 1/2$, which is close to the values expected for the subsonic turbulence in the ICM (e.g., Ryu et al. 2008; Porter et al. 2015).

The inserted box in Figure 1(a) shows the development and variation of v_{rms} with our sporadic forcing. Colored and white parts mark the periods during which the forcing is turned on and off, respectively. As shown with different colored lines, the evolution of v_{rms} is insensitive to the strength of the initial background magnetic field, B_0 , as well as to numerical resolution (not shown).

In the discussion of results below, we consider the Coma cluster as the representative cluster. Considering the core radius of the Coma cluster is $r_c \simeq 300$ kpc (e.g., Briel et al. 1992; Ogcaan & Brüggen 2013),

the simulation box size is regarded to be $L_0 = 4$ Mpc; then, the grid resolution is $\Delta x \equiv L_0/N_g = 3.9 - 31.25$ kpc. The peak scale of the velocity forcing is close to $\sim L_0/8 = 500$ kpc, typical size of subclumps in major mergers (e.g., Ha et al. 2018a). We assign $c_s = 1.5 \times 10^3 \text{ km s}^{-1}$, appropriate for the Coma’s ICM temperature of $kT = 8 - 9 \text{ keV}$ (e.g., Sato et al. 2011); then the unit time corresponds to $t_0 = L_0/c_s = 2.6$ Gyrs, and hence our simulations ran up to $t_{\text{end}} = 13$ Gyrs, close to the age of the universe. Finally, assuming that ρ_0 represents the ion number density of $3.5 \times 10^{-3} \text{ cm}^{-3}$ at the Coma cluster center (e.g., Briel et al. 1992), the magnetic field unit corresponds to $\sim 5 \times 10^{-5} \text{ G}$, and hence B_0 is equivalent to $\sim 5 \times 10^{-14} - 5 \times 10^{-9} \text{ G}$.

3. RESULTS

3.1. Amplification of Seed Magnetic Fields

Figure 1 illustrates turbulence dynamo in simulations with different initial B_0 and different numerical resolutions. The left panel shows that the saturation level of the magnetic energy, E_{mag} , at t_{end} depends on B_0 . The right panel demonstrates that the growth of E_{mag} depends rather strongly on numerical resolution. The evolution of E_{mag} looks different from that in simulations for turbulence dynamo in uniform media with continuous driving of turbulence. (see, e.g., Figure 1 of Porter et al. 2015), owing partly to the sporadic nature of the forcing and partly to the stratification of the background medium. After the quick initial exponential growth during $t \lesssim 0.5$, the follow-up growth is also approximated to be exponential rather than linear. This second exponential growth is slower than the initial growth, and hence the final E_{mag} depends on the initial B_0 in simulations of 512^3 grid zones as shown in Figure 1(a), and also on the grid resolution as shown in Figure 1(b).

If the amplification of magnetic field, B , during the second exponential growth stage is modeled as $\langle B \rangle \propto \exp(t/\tau_{\text{growth}})$ [dashed lines in Figure 1 (b)], then the growth time scale can be fitted to $\tau_{\text{growth}} \approx 10^2 \Delta x + 0.13$ in the computational units. In the physical units appropriate for the Coma cluster, this corresponds to

$$\tau_{\text{growth}} \approx 0.066 \left(\frac{\Delta x}{\text{kpc}} \right) + 0.34 \text{ Gyrs.} \quad (2)$$

In the highest resolution simulation with $\Delta x = 3.9$ kpc (1024^3 grid zones), $\tau_{\text{growth}} \approx 0.6$ Gyrs; hence, $\langle B \rangle$ can grow by a factor of 10^7 during ~ 10 Gyrs. With the initial seed fields of $B_0 \approx 10^{-15} \text{ G}$, which is close to the lower bound of the void magnetic field (see the Introduction), the mean magnetic field of $\langle B \rangle \sim \mu\text{G}$ would develop within ~ 10 Gyrs, only if the grid size is sufficiently small, such as $\Delta x \lesssim 2$ kpc.

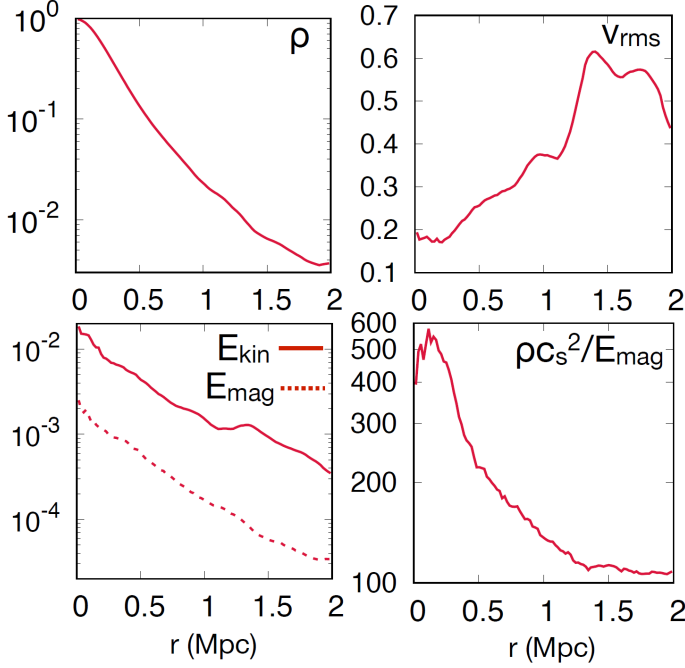


Figure 3. Radial profiles of ρ , v_{rms} , E_{kin} and E_{mag} , and $(\rho c_s^2)/E_{\text{mag}}$ at $t = 4.6$ in the high-resolution simulation of 1024^3 grid zones with the initial background magnetic field strength of $B_0 = 10^{-8}$. While the quantities are plotted in the simulation units, the radius from the center is given in units of Mpc, adopting $L_0 = 4$ Mpc.

The Coulomb mean-free path between collisions is given as $\lambda_{\text{Coul}} \sim 0.3 T_{\text{keV}}^2 / n_{-3}$ kpc, where T_{keV} is the ICM temperature in keV and n_{-3} is the particle number density in units of 10^{-3} cm^{-3} (see, e.g., Narayan & Medvedev 2001). It is of order of kpc in the cluster core, while it is as large as tens of kpc in the outskirts. However, it is likely that the effective mean-free path is reduced by plasma instabilities (e.g., Brunetti & Jones 2014). In fact, analyzing the fluctuations in the Chandra data of the Coma cluster, Zhuravleva et al. (2019) recently argued that the effective mean-free path would be smaller by two orders of magnitude than the Coulomb value. Our results indicate that if the fluid description of the ICM is valid down to the scale of the order of kpc, turbulence dynamo should be able to amplify the primordial magnetic field of as weak as $\sim 10^{-15}$ G to the cluster magnetic field of $\sim \mu\text{G}$ within the age of the universe.

As described in the Introduction, there have been cosmological simulation studies in which the amplification of magnetic fields via turbulence dynamo was examined in the context of the LSS formation (e.g., Vazza et al. 2014; Marinacci et al. 2015; Vazza et al. 2018). So far those simulations failed to reproduce a sufficient amplification of B on cluster scales. This should be partly because their spatial resolution of several kpc is not fine

enough, and partly because their numerical codes are only second-order accurate. Moreover, those simulations employed either AMR (adaptive mesh refinement) or moving mesh techniques in order to achieve high resolutions inside clusters. We expect that numerical details, such as the code accuracy and the grid structure, would affect the amplification of B . In particular, although not shown here, we found that the high-order WENO code effectively has the resolution enhancement of a factor of two, compared to second-order accurate codes such as the TVD code (Ryu & Jones 1995; Kim et al. 1999), when the same number of grid zones is used.

However, we should note that the current simulations, which were performed in an idealized setup with one model cluster in a periodic box, does not include effects involved in full cosmological simulations, such as the expansion of the universe and realistic mergers during the hierarchical formation of the LSS of the universe. Hence, our conclusion on the capability of turbulence dynamo for the amplification of B in galaxy clusters should be verified in the future with full cosmological simulations of resolution $\Delta x \sim 1$ kpc or so, possibly in a (non-AMR) uniform grid structure, using codes of high accuracy.

Figure 2 shows the $B - \rho$ relation in the 1024^3 simulation at $t = 4.6$, the epoch when M_{turb} is close to $1/2$ [Figure 1(b)]. In previous simulations in uniform media with continuous driving, supersonic turbulence, which is relevant for the environment of molecular clouds, gives the scaling relation of $B \propto \rho^\kappa$ with $\kappa = 0.3 \sim 0.5$ (e.g., Padoan & Nordlund 1999; Ostriker et al. 2001). For subsonic turbulence of $M_{\text{turb}} \lesssim 1$ with weak seed fields, the correlation between B and ρ is rather weak with small correlation coefficient, although the coefficient value depends on M_{turb} and B_0 , as well as the details of forcing (e.g., Wu et al. 2009; Yoon et al. 2016). Cosmological structure-formation simulations, in particular, those without radiative cooling and feedback processes, on the other hand, produced the relation close to $B \propto \rho^{2/3}$ for galaxy clusters (e.g., Vazza et al. 2014; Marinacci et al. 2015), implying that possibly compression would have played a significant role on the amplification of B . Our simulations give a relation close to $B \propto \rho^{1/3}$. We interpret that the $B \propto \rho^{1/3}$ scaling is a consequence of turbulence dynamo, but also affected by the stratification of the background medium.

Figure 3 shows the radial profiles of $\langle \rho \rangle$, $\langle v^2 \rangle^{1/2}$, $\langle (1/2) \rho v^2 \rangle$ and $\langle (1/2) B^2 \rangle$, and $\langle \rho c_s^2 \rangle / \langle (1/2) B^2 \rangle$, again in the 1024^3 simulation at $t = 4.6$. The average was calculated over a thin shell at the given radius. Although the rms flow velocity increases from the core to the outskirts, the kinetic and magnetic energies decrease due to

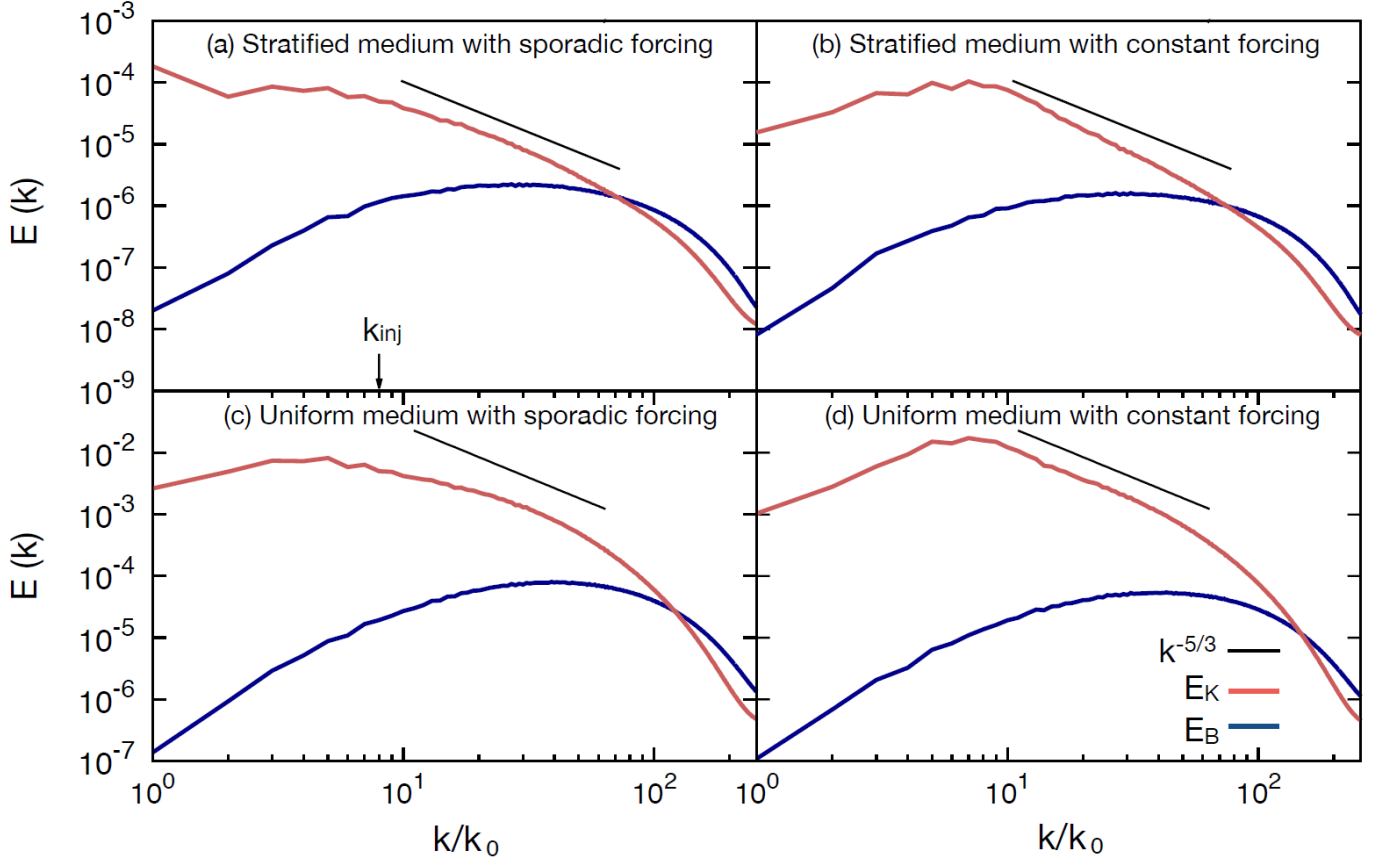


Figure 4. Comparison of the energy power spectra in turbulence simulations with different setups: (a) in a radially stratified medium with a sporadic forcing, (b) in a radially stratified medium with a continuous forcing, (c) in a uniform medium of initially $\rho = 1$ with a sporadic forcing, and (d) in a uniform medium with a continuous forcing. The red and blue lines show the kinetic energy spectrum, $E_K(k)$, and the magnetic energy spectrum, $E_B(k)$, respectively. The black lines draw the Kolmogorov slope. Here, $k_0 = 2\pi/L_0$. In all the cases, results from the simulations of 512^3 grid zones with $B_0 = 10^{-6}$ at $t = 4.6$ are presented; $k_{\text{inj}} = 8k_0$ and v_{rms} of each model are identical.

the density stratification, as also shown in cosmological structure-formation simulations (e.g., Vazza et al. 2017; Domínguez-Fernández et al. 2019). The decrease of v_{rms} at large radii ($r > 1.3$ Mpc) should be the consequence of the periodic boundary adopted in the simulation. In the simulation shown here, the magnetic field has amplified to the level of $E_{\text{mag}} \sim (1/10)E_{\text{kin}}$ throughout the cluster. In the outskirts, the ratio of the effective thermal energy, $E_{\text{th}} = \rho c_s^2$, and the magnetic energy (i.e., the plasma beta) approaches ~ 100 , close to the value expected in the ICM (e.g., Ryu et al. 2008; Brunetti & Jones 2014).

3.2. Scale of Magnetic Fields

The amplification of the strength of B is one aspect of turbulence dynamo, while the growth of the coherence scale of B is another aspect (e.g., Cho & Ryu 2009). To examine the scale issue, the kinetic and magnetic energy power spectra from a simulation with 512^3 grid zones are shown in Figure 4(a). They are compared with those for turbulences differently generated: (b) a radi-

ally stratified medium with a continuous forcing, (c) a uniform medium with a sporadic forcing, and (d) a uniform medium with a continuous forcing. The injection scale of the forcing, k_{inj} , is the same and v_{rms} is tuned to be similar at the time shown, $t = 4.6$, in all four models.

In the case of a uniform background with a continuous forcing [Figure 4(d)], turbulence exhibits the expected behaviors; that is, while the kinetic energy power spectrum, $E_K(k)$, has the peak around k_{inj} , the magnetic energy power spectrum, $E_B(k)$, has the peak at a scale a few times smaller than the injection scale (e.g., Cho et al. 2009; Porter et al. 2015). With our model for the sporadic forcing, $t = 4.6$ corresponds to an epoch of decaying turbulence, and hence the peak of $E_B(k)$ is expected to migrate to a larger scale (e.g., Campanelli 2007). In addition, the stratification of the background medium induces powers in $E_K(k)$ on the cluster scale (e.g., Vazza et al. 2014), and hence the peak of $E_B(k)$ shifts to larger scales, compared to the case with the uniform background. Combining the two effects, the peak

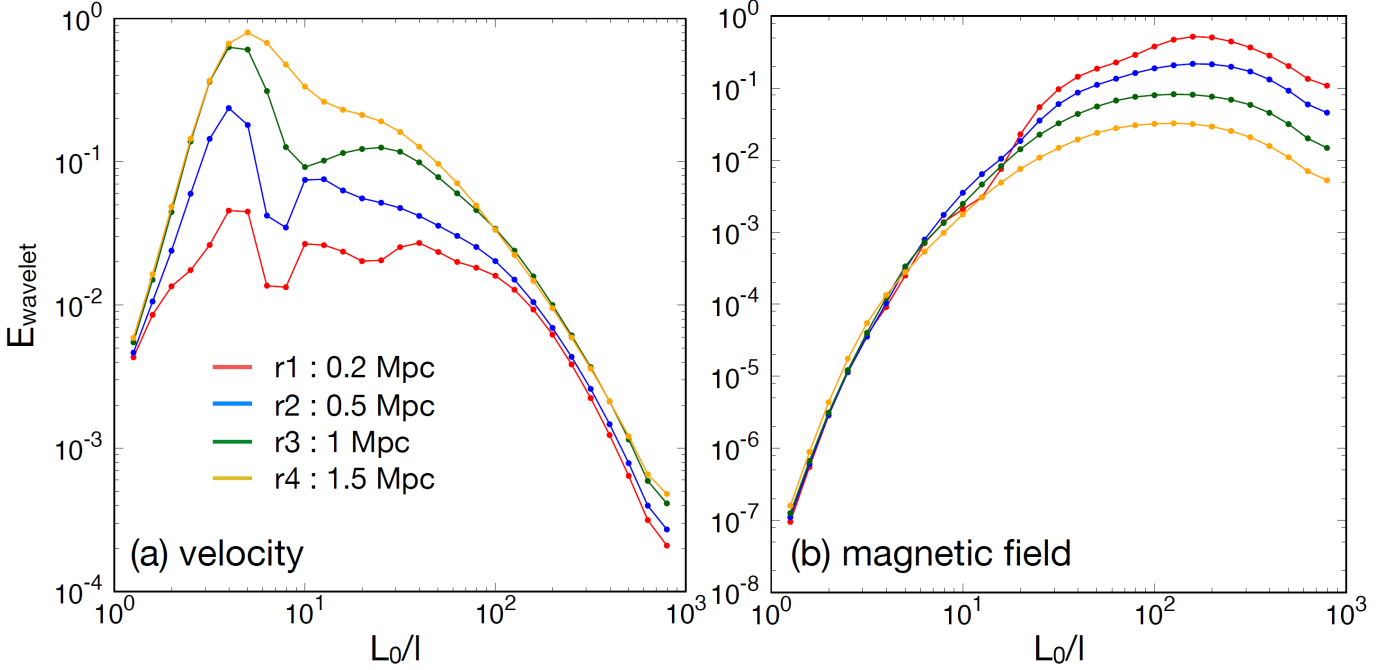


Figure 5. Wavelet power spectra of the flow velocity (a) and the magnetic field (b) as a function of the effective wavenumber of the filtering scale, L_0/l , at four different radii ($r_i = 0.2, 0.5, 1.0$, and 1.5 Mpc, shown with different colors) from the center, for the simulation same as in Figure 4(a). $L_0 = 4$ Mpc is adopted. The vertical scales of the plots are arbitrary.

of $E_B(k)$ in panel (a) indeed locates at a scale larger than that in panel (d). However, we find that the shift is not dramatic, just a factor of two or so; the peak scale of $E_B(k)$ is at $k/k_0 \simeq 20$ in panel (a), while at $k/k_0 \simeq 40$ in panel (d).

Figure 4(a) shows that $E_K(k)$ and $E_B(k)$ cross at the scale of $k/k_0 \approx 70$ (60 kpc for $L_0 = 4$ Mpc). This crossing has been also seen in some of high-resolution cosmological simulations (e.g., Domínguez-Fernández et al. 2019). On this scale, the turbulence eddy speed roughly equals the Alfvén speed, and hence it is often called the Alfvén scale, l_A . Below this scale, the Maxwell stress is larger than the Reynolds stress and the flow becomes MHD. The Alfvén scale increases slightly with time in our simulations; that is, l_A becomes somewhat larger in later stage. In our model cluster, l_A is larger by an order to magnitude or more than the Coulomb collision scale, λ_{Coul} , while previously $l_A \lesssim \lambda_{\text{Coul}}$ was often expected (e.g., Brunetti & Jones 2014).

While the power spectrum in Figure 4 tells us the scale of B throughout the whole computational domain, the scale in clusters should differ at different radii from the center due to the density stratification. One way to examine the position-dependence of the scale of turbulence is through the so-called wavelet analysis (e.g., Farge 1992; Shi et al. 2018). We calculated a wavelet power spectrum with the Mexican-hat wavelet. Then,

the wavelet function is expressed as

$$\psi_{l,\mathbf{x}'}(\mathbf{x}) \propto l^{-\frac{3}{2}} \left(3 - \frac{|\mathbf{x} - \mathbf{x}'|^2}{l^2} \right) \exp \left(-\frac{|\mathbf{x} - \mathbf{x}'|^2}{2l^2} \right), \quad (3)$$

where l is the filtering scale. The wavelet coefficient of a fluid quantity, $f(\mathbf{x})$, is computed as

$$\hat{F}_l(\mathbf{x}) = \int f(\mathbf{x}') \psi_{l,\mathbf{x}'}(\mathbf{x}) d^3\mathbf{x}', \quad (4)$$

and the wavelet power spectrum is given as $E_{\text{wavelet}}(\mathbf{x}) \propto l^{-2} |\hat{F}_l(\mathbf{x})|^2$. Figure 5 shows (a) the wavelet power spectrum, calculated as $l^{-2} (|\hat{V}_{xl}(\mathbf{x})|^2 + |\hat{V}_{yl}(\mathbf{x})|^2 + |\hat{V}_{zl}(\mathbf{x})|^2)$, for \mathbf{v} and (b) the wavelet power spectrum calculated similarly for \mathbf{B} , as a function of L_0/l , at four different radii ($r_i = 0.2, 0.5, 1.0$, and 1.5 Mpc), for the simulation same as in Figure 4(a). The power spectra averaged over a thin shell at the given radius are shown.

The wavelet power spectrum for \mathbf{v} demonstrates that as we move from the core (red line) to the outskirts (yellow line), the relative fraction of the power of turbulent flow motions at large l , specifically, at $l \gtrsim L_0/10$, increases. The same trend was previously seen in cosmological structure-formation simulations (e.g., Shi et al. 2018). Accordingly, the peak scale in the wavelet power spectrum for \mathbf{B} also increases with the radius. While the peak is around $L_0/l \approx 150$ at the core of $r = 0.2$ Mpc, it is found around $L_0/l \approx 100$ at the outskirts of $r = 1 - 1.5$ Mpc. This indicates that the coherence length of \mathbf{B} increases from the core to the outskirts, but

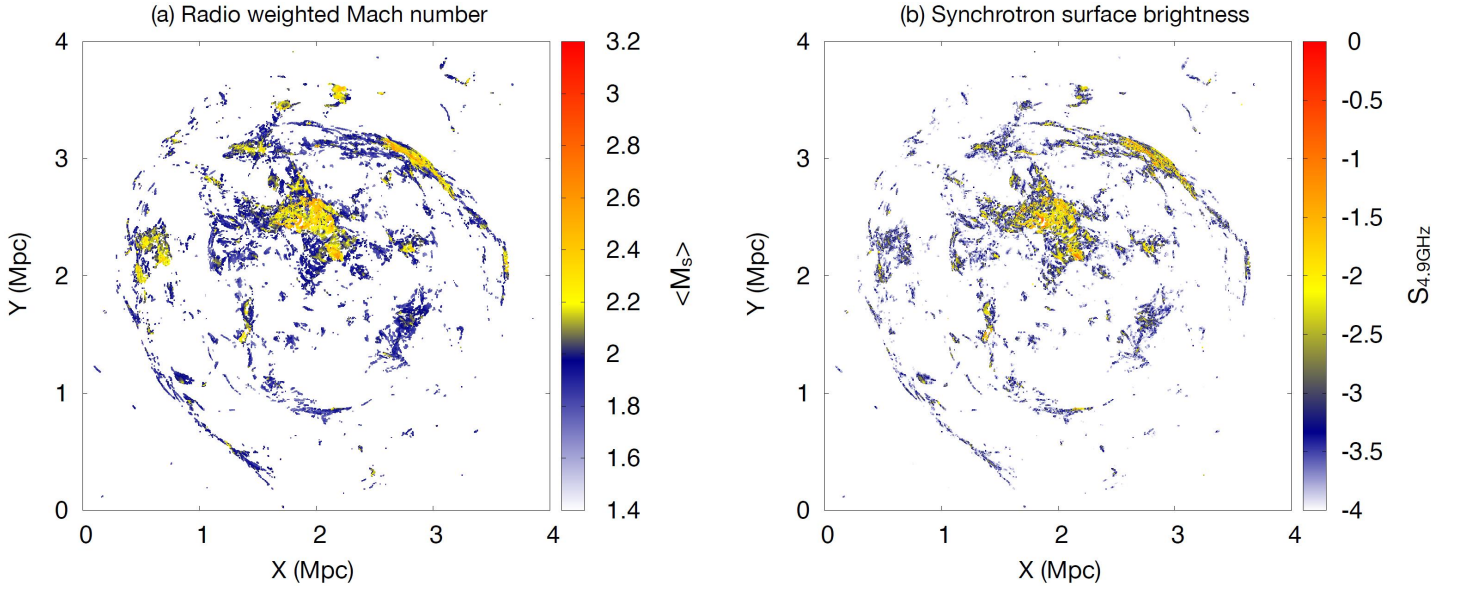


Figure 6. Maps projected along the line of sight (z -direction): (a) the shock Mach number weighted by synchrotron emissivity at 4.9 GHz, $\langle M_s \rangle$, and (b) the synchrotron surface brightness at 4.9 GHz, $S_{4.9}$, in the high-resolution simulation of 1024^3 grid zones at $t = 4.6$. The synchrotron emission was computed only at shock zones. See the text for the details of the calculations of $\langle M_s \rangle$ and $S_{4.9}$.

the increment is expected to be less than a factor of two in our simulations.

3.3. Turbulent Magnetic Fields in Radio Relics

We point that the peak scale of $E_B(k)$ is ~ 200 kpc and the most energy containing scale, that is, the peak scale of $kE_B(k)$, is ~ 65 kpc in Figure 4(a). The peak of the wavelet power spectrum for \mathbf{B} is at $l \approx 40$ kpc in the cluster outskirts, as shown in Figure 5(b). All these are smaller than the size of giant radio relics by an order of magnitude or more (see the Introduction). It is not clear, however, how statistical quantities, like these peak scales, would be manifested in real observations. Hence, we here examine the structures of synchrotron polarization vectors in simulated radio relics, due to turbulence-generated magnetic fields, specifically including the effects of the shock compression of the magnetic fields.

To that end, we first identified shock zones (actually grid zones that are parts of shock surfaces) in the simulated cluster with the algorithm described in Ryu et al. (2003) and Park & Ryu (2019). The shock Mach number, M_s , was calculated using a formula from the jump condition for isothermal flows in Equation (9) of Park & Ryu (2019). In fact, it is almost identical to that of hydrodynamic flows, $M_s \equiv \sqrt{\chi}$ (where χ is the density compression ratio across the shock), since the magnetic energy is substantially smaller than the kinetic energy in ICM shocks.²

We estimated the population of synchrotron-emitting cosmic-ray (CR) electrons as follow. CR electrons are assumed to be produced via diffusive shock acceleration (DSA) at “quasi-perpendicular” shocks with $\theta_{Bn} \gtrsim 45^\circ$, the obliquity angle between the upstream background magnetic field direction and the shock normal (e.g., Guo et al. 2014; Kang et al. 2019). The fraction of quasi-perpendicular shocks is $\sim 70\%$ in our simulations, which is naturally expected with turbulence-generated ICM magnetic fields. The test-particle DSA model is assumed, because most of ICM shocks are weak with $M_s \lesssim 3-4$ (e.g., Ryu et al. 2003; Ha et al. 2018b); then, the energy distribution of CR electrons can be modeled with a power-law form, $n_{\text{CR}} = n_0 \gamma^{-p}$ for $\gamma > \gamma_{\text{min}}$, where γ is the Lorentz factor and the DSA slope is $p = (2M_s^2 + 2)/(M_s^2 - 1)$ (e.g., Drury 1983).

Although the detailed processes of CR electron acceleration at ICM shocks are yet to be understood (e.g., Guo et al. 2014; Kang et al. 2019), the acceleration efficiency η_e , the fraction of the shock energy transferred to CR electrons, is expected to increase with the shock Mach number. We adopted a rather simple scaling relation, $\eta_e \propto M_s$, for weak ICM shocks with $M_s \lesssim 4$. We also assumed that the electron acceleration is effective only in quasi-perpendicular shocks with $M_s \geq 1.2$, and we choose $\gamma_{\text{min}} = 300$. The quantitative estimates of synchrotron emission by shock-accelerated CR electrons should depend on the details of the adopted model parameters. However, the main conclusion we will draw below should not be very sensitive to them, because we

² Most of identified shocks are fast shocks by the same reason.

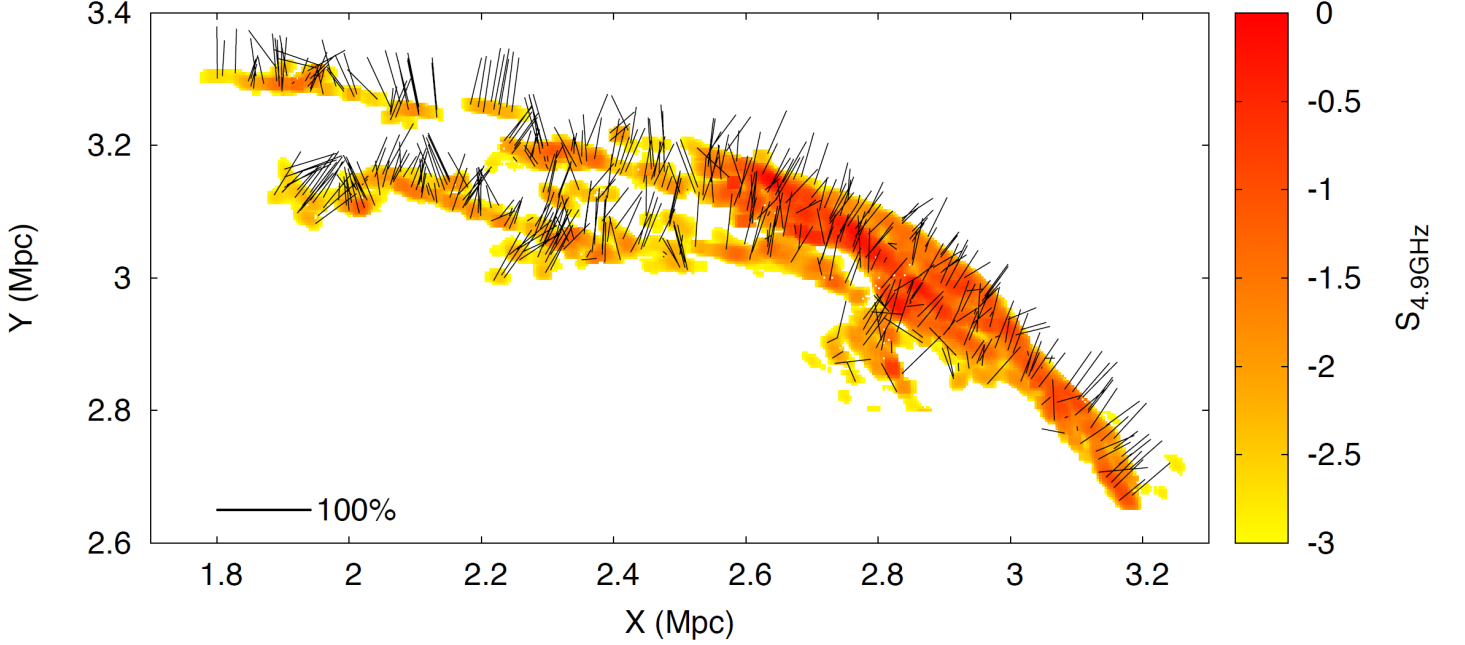


Figure 7. Zoom-in image of an upper-right part of Figure 6(b) for the synchrotron surface brightness, $S_{4.9}$, which mimics an observed giant radio relic. To match the resolution of radio observations, $S_{4.9}$ was smoothed over $\sim 20 \times 20$ kpc². The black lines denote the polarization electric vectors, and their length scales with the polarization fraction.

focus on the structures of polarization vectors of synchrotron emission, instead of the flux level.

We then calculated the synchrotron surface brightness. The synchrotron volume emissivity at frequency ν is given as $j_\nu \propto n_0 B_\perp^{(p+1)/2} \nu^{-(p-1)/2}$, where B_\perp is the strength of the magnetic field component perpendicular to the line of sight (LoS). The Stokes parameters of the volume emissivity were calculated, using, for instance, $J_F(p)$ and $J_G(p)$ in Chapter 19 of Shu (1992), in each shock zone with B in the zone. The Stokes parameters of synchrotron surface brightness, I_ν , Q_ν , and U_ν , were calculated by integrating the emissivity along LoSs, assuming that the diffuse ICM is optically thin to the synchrotron radiation.

Figure 6 shows (a) the projected shock Mach number, $\langle M_s \rangle$, weighted with the synchrotron emissivity at 4.9 GHz, along LOSs and (b) the synchrotron surface brightness at 4.9 GHz, $S_{4.9}$, in the 1024³ simulation at $t = 4.6$. We note that the maps are produced with synchrotron emission only from shock zones; that is, the synchrotron radiation from the postshock zones behind the shock surface is not included. The grid size of this simulation is $\Delta x = 3.9$ kpc, while the width of the synchrotron-emitting region behind the shock at $\nu = 4.9$ GHz is $\Delta l_{4.9} \sim 10$ kpc, if the postshock magnetic field strength is $\sim 1 \mu$ G and the postshock flow speed is ~ 500 km s⁻¹ (e.g., Kang & Ryu 2015). Hence, the map of the surface brightness may not be the exact reproduction of observed radio relics. Yet, the figure shows that shocks formed in our simulations are weak with the

projected Mach number of $\langle M_s \rangle \lesssim 3$. The synchrotron surface brightness reveals shell-like structures, as previously shown in full cosmological simulations (e.g., Skillman et al. 2013; Wittor et al. 2017).

The thin elongated part in the upper-right region of the shell-like structures in Figure 6 looks similar to observed giant radio relics. It is zoomed in and shown in Figure 7; the surface brightness profile shown was smoothed over 4×4 grid zones, or $\sim 20 \times 20$ kpc², to match the resolution of radio observations (e.g., van Weeren et al. 2010, 2016). The black lines represent the electric field vectors of polarized radiation; the fraction of linear polarization was calculated with $\sqrt{Q_\nu^2 + U_\nu^2}/I_\nu$, and the angle χ was calculated with $\tan 2\chi = U_\nu/Q_\nu$.

The average Mach number of the mock radio relic in Figure 7 is ~ 2.3 , which is a bit smaller than, but close to, for instance, those inferred from the observed radio spectral index of the Sausage and Toothbrush relics (e.g., van Weeren et al. 2016; Hoang et al. 2017). The projected Mach number, however, is not uniform over the whole structure, as can be seen in Figure 6(a). Rather it has a range of $\langle M_s \rangle \sim 1.6 - 2.5$. This is because the shock surfaces are not smooth, but composed of parts with different Mach numbers. This is in good agreement with the characteristics of ICM shocks formed in full cosmological structure-formation simulations (e.g., Hong et al. 2015; Ha et al. 2018a).

The polarization vectors of the mock radio relic look fairly organized, but not as well as those, for instance, in the Sausage and Toothbrush relics (e.g., van Weeren et

al. 2010, 2012). The polarization fraction along the relic front is on average $\sim 45\%$, which is smaller than that of the Sausage relic ($\sim 50 - 60\%$) but a bit larger than that of Toothbrush ($\sim 40\%$). However, the polarization angle between the polarization electric vectors and the shock normal is on average $\langle \vartheta_{\text{En}} \rangle \sim 16^\circ$, about twice larger than that of the Sausage relic.³ Although not shown here, we examined a number of mock radio relics from our simulations; the average polarization fraction is typically $\lesssim 40\%$, and the average polarization angle is $\langle \vartheta_{\text{En}} \rangle \gtrsim 20^\circ$. That is, our results indicate that with turbulence-generated magnetic fields in clusters, the highly organized structures of polarization vectors, such as those in the Sausage relic, would be difficult to be explained; the compression of the transverse components of turbulence-generated magnetic fields by weak ICM shocks may not be large enough to reproduce the observed levels of quasi-perpendicular obliquity angles of giant radio relics. This implies that for some observed radio relics, there may have been the pre-existing structures of magnetic fields, organized over the whole length scale of the radio relics.

We note that in the so-called reacceleration model for giant radio relics, ICM shocks are conjectured to sweep through the remnant bubbles of dead radio jets that contain fossil relativistic electrons with $\gamma \lesssim 300$ (e.g., Kang et al. 2012, 2017). This model was proposed mainly to explain the discrepancy between two kinds of shock Mach numbers inferred from radio and X-ray observations, and also to alleviate the problem of low acceleration efficiency in weak shocks and the low frequency of merging clusters with detected radio relics (Kang 2016). However, if pre-existing magnetic fields are also required, their origin should be further investigated, but that is beyond the scope of this paper.

4. SUMMARY

Magnetic fields in galaxy clusters, at least in the outskirts, are conjectured to be originated by small-scale dynamo due to the turbulence induced during the hierarchical formation of the LSS of the universe. Yet, the characteristics of the dynamo has not been fully understood, because the turbulence in the ICM differs in some aspects from those in other astrophysical environments such as molecular clouds and star-forming

regions. For instance, the turbulence is induced in the highly stratified ICM due to the gravity; also it is driven sporadically by mergers of sub-clusters. And most of all, the turbulence is subsonic with turbulence Mach number $M_{\text{turb}} < 1$.

To estimate quantitative measures for turbulence and magnetic field amplification in the ICM, we performed a set of MHD simulations. Instead of running cosmological structure-formation simulations, we set up a model cluster with a radially stratified profile in a controlled periodic volume, and induced turbulence mimicking a series of sporadic merger events. A newly developed, high-order-accurate MHD code was employed. We then analyzed the characteristics of turbulence dynamo and the properties of resulting magnetic fields.

Our main findings can be recapitulated as follows.

1. Turbulence dynamo should be able to generate the cluster magnetic fields of $\sim \mu\text{G}$ from the primordial seed fields of $\sim 10^{-15} \text{ G}$ or so within the age of the universe, if the MHD description of the ICM can be extended down to the scale of $\sim \text{kpc}$ or so.

2. With the compression of the transverse components of turbulence-generated magnetic fields by weak ICM shocks, some of the observed properties of synchrotron polarization in radio relics may be explained, but the highly organized structures of polarization vectors like those observed in the Sausage relic are difficult to be reproduced.

Finally, we note that the simulations described in this paper adopted an idealized setup with one model cluster in a periodic box, and hence did not include cosmological effects, such as the expansion of the universe and realistic mergers during the hierarchical formation of galaxy clusters. Hence, our findings should be eventually verified through full cosmological MHD simulations with high-resolutions of $\Delta x \sim 1 \text{ kpc}$ or so. Although such simulations are beyond the capacity of current super-computing resources, they should be realizable in a near future.

We thank the anonymous referee for constructive comments that help us improve this paper. This work was supported by the National Research Foundation (NRF) of Korea through grants 2016R1A5A1013277, 2017R1A2A1A05071429, and 2017R1D1A1A09000567.

REFERENCES

- Batchelor, G. 1950, Proc. R. Soc. Lond. A, 201, 405
- Briel U. G., Henry J. P., & Böhringer H., 1992, A&A, 259,

³ We estimated the angle for the Sausage relic by ourselves using the polarization vectors in Figure 3 of van Weeren et al. (2010).

- Brüggen, M., Bykov, A., Ryu, D., & Röttgering, H. 2012, *SSRv*, 166, 187
- Brunetti, G. & Jones, T. W. 2014, *IJMPD*, 23, 1430007
- Brunetti, G. & Lazarian, A. 2007, *MNRAS*, 378, 245
- Campanelli, L. 2007, *PhRvL*, 98, 251302
- Cavaliere, A., & Fusco-Femiano, R. 1976, *A&A*, 49, 137
- Cho, J. & Ryu, D. 2009, *ApJL*, 705, L90
- Cho, J. & Vishniac, E. 2000, *ApJ*, 538, 217
- Cho, J., Vishniac, E. T., Beresnyak, A., Lazarian, A., & Ryu, D. 2009, *ApJ*, 693, 1449
- Domínguez-Fernández, P., Vazza, F., Brüggen, M., & Brunetti, G. 2019, *MNRAS*, 486, 623
- Drury, L. O. 1983, *Rep. Progr. Phys.*, 46, 973
- Farge M. 1992, *Annu. Rev. Fluid Mech.*, 24, 395
- Feretti L., Giovannini G., Govoni F., & Murgia M., 2012, *A&A Rv*, 20, 54
- Govoni, F. & Feretti, L. 2004, *IJMPD*, 13, 1549
- Guo, X., Sironi, L., & Narayan, R. 2014, *ApJ*, 794, 153
- Ha, J.-H., Ryu, D., & Kang, H. 2018, *ApJ*, 857, 26
- Ha, J.-H., Ryu, D., Kang, H., & van Marle, A. J. 2018, *ApJ*, 864, 105
- Hoang, D. N., Shimwell, T. W., Stroe, A., et al. 2017, *MNRAS*, 471, 1107
- Hong, S. E., Kang, H., & Ryu, D. 2015, *ApJ*, 812, 49
- Jabbari, S., Brandenburg, A., Losada, L. R., et al. 2014, *A&A*, 568, A112
- Jiang, G.-S. & Shu, C.-W. 1996, *J. Comput. Phys.*, 126, 202
- Jiang, G.-S. & Wu, C.-C. 1999, *J. Comput. Phys.*, 150, 561
- Kang, H. 2016, *JKAS*, 49, 83
- Kang H. & Ryu, D. 2015, *ApJ*, 809, 186
- Kang H., Ryu, D., & Jones, T. W. 2012, *ApJ*, 756, 97
- Kang H., Ryu, D., & Jones, T. W. 2019, *ApJ*, 840, 42
- Kang H., Ryu, D., & Ha, J. H. 2019, *ApJ*, 876, 79
- Kazantsev, A. P. 1968, *JETP*, 26, 1031
- Kim J., Ryu, D., Jones, T. W., & Hong S. 1999, *ApJ*, 514, 506
- Kunz, M. W., Schekochihin, A. A., Cowley, S. C., Binney, J. J., & Sanders, J. S. 2010, *MNRAS*, 410, 2446
- Marinacci, F., Vogelsberger, M., Mocz, P., & Pakmor, R. 2015, *MNRAS*, 453, 3999
- Miniati, F. 2015, *ApJ*, 800, 60
- Mac Low, M.-M. 1999, *ApJ*, 524, 169
- Narayan, R. & Medvedev, M. V. 2001, *ApJL*, 562, L129
- Neronov, A. & Vovk, I. 2010, *Sci*, 328, 73
- Ogrea, G. A. & Brüggen, M. 2013, *MNRAS*, 433, 1701
- Ostriker, E. C., Stone, J. M., & Gammie, C. F. 2001, *ApJ*, 546, 980
- Padoan, P. & Nordlund, Å. 1999, *ApJ*, 526, 279
- Park, J. & Ryu, D. 2019, *ApJ*, 875, 2
- Planck Collaboration 2016, *A&A*, 594, A19
- Porter, D. H., Jones, T. W., & Ryu, D. 2015, *ApJ*, 810, 93
- Roberg-Clark, G. T., Drake, J. F., Reynolds, C. S., & Swisdak, M. 2016, *ApJL*, 830, L9
- Ryu, D. & Jones, T.W. 1995, *ApJ*, 442, 228
- Ryu, D., Kang, H., Cho, J., & Das, S. 2008, *Sci*, 320, 909
- Ryu D., Kang H., Hallman E., & Jones T. W. 2003, *ApJ*, 593, 599
- Ryu, D., Miniati, F., Jones, T.W., & Frank, A. 1998, *ApJ*, 509, 244
- Ryu, D., Scheicher, D. R. G., Treumann, R. A., Tsagas, C. G., & Widrow, L. M. 2012, *SSRv*, 166, 1
- Sato, T., Matsushita, K., Ota, N., et al. 2011, *PASJ*, 63, S991
- Schekochihin, A. A., Cowley, S. C., Taylor, S. F., Maron, J. L., & McWilliams, J. C. 2004, *ApJ*, 612, 276
- Shi, X., Nagai, D., & Lau, E. T. 2018, *MNRAS*, 481, 1075
- Shu, F. H., 1992, *The Physics of Astrophysics, Volume I, Radiation* (Mill Valley: University Science Books)
- Skillman, S. W., Xu, H., Hallman, E. J., et al. 2013, *ApJ*, 765, 21
- Stone J. M., Ostriker E. C., & Gammie C. F. 1998, *ApJL*, 508, L99
- Tavecchio, F., Ghisellini, G., Foschini, L., et al. 2010, *MNRAS*, 406, L70
- van Weeren, R. J., Brunetti, G., Brüggen, M., et al. 2016, *ApJ*, 818, 204
- van Weeren, R. J., de Gasperin, F., Akamatsu, H., et al. 2019, *SSRv*, 215, 16
- van Weeren, R. J., Röttgering, H. J. A., Brüggen, M., & Hoeft, M. 2010, *Sci*, 330, 347
- van Weeren, R. J., Röttgering, H. J. A., Intema, H. T., et al. 2012, *A&A*, 546, A124
- Vazza, F., Brüggen, M., Gheller, C., & Wang, P. 2014, *MNRAS*, 445, 3706
- Vazza, F., Brunetti, G., Brüggen, M., & Bonafede, A. 2018, *MNRAS*, 474, 1672
- Vazza, F., Jones, T. W., Brüggen, M., et al. 2017, *MNRAS*, 464, 210
- Widrow, L. M., Ryu, D., Schleicher, D. R. G., et al. 2012, *SSRv*, 166, 37
- Wittor, D., Vazza, F., & Brüggen, M. 2017, *MNRAS*, 464, 4448
- Wu, Q., Kim, J., Ryu, D., Cho, J., & Alexander, P. 2009, *ApJL*, 705, L86
- Yoon, H., Cho, J., & Kim, J. 2016, *ApJ*, 831, 85
- Zhuravleva, I., Churazov, E., Schekochihin, A. A., et al. 2019, *Nature Astron.*, in press (arXiv:1906.06346)